energies

MDPI

Article

Model Predictive Control for Three-Phase, Four-Leg Dynamic Voltage Restorer

Decan Liu [1], Huaying Zhang [2], Xiaorui Liang [2,*] and Shicong Deng [2]

[1] College of Electrical Engineering, Sichuan University, Chengdu 610017, China; liudecan@stu.scu.edu.cn
[2] China Southern Power Grid, Guangzhou 510663, China; zhytgyx@163.com (H.Z.); donghulang@163.com (S.D.)
* Correspondence: xrliang@mail.tsinghua.edu.cn

Abstract: Dynamic voltage restores (DVRs) are usually used to mitigate the effect of voltage sag and guarantee sufficient power supply for sensitive loads. However, three-phase voltage cannot be compensated to the desired balance voltage under unbalanced three-phase loads by traditional DVRs with a three-phase, three-leg inverter. To address this problem, a three-phase, four-leg inverter-based DVR is first introduced in this paper, and then the state space model in its continuous form and discrete form are established, respectively. A two-step predictive method is proposed for the prediction of the output voltage in each switching state by the established voltage prediction model. Finite-control-set model predictive control (MPC) is developed to be used in the three-phase, four-leg inverter-based DVR. Its dynamic response is effectively improved by the proposed MPC method under various voltage sag conditions. The proposed DVR control strategy is validated via MATLAB/Simulink-R2022b simulations, which demonstrate its effectiveness in voltage compensation under various sag conditions.

Keywords: DVR; three-phase, four-leg inverter; SOGI; FCS-MPC

Citation: Liu, D.; Zhang, H.; Liang, X.; Deng, S. Model Predictive Control for Three-Phase, Four-Leg Dynamic Voltage Restorer. *Energies* **2024**, *17*, 5622. https://doi.org/10.3390/en17225622

Academic Editor: Adolfo Dannier

Received: 15 September 2024
Revised: 31 October 2024
Accepted: 7 November 2024
Published: 10 November 2024

1. Introduction

Voltage sag is a typical power quality issue in modern power grids [1,2], and it can significantly affect the stability of sensitive loads. Dynamic voltage restorers (DVRs) have been widely implemented as an effective solution to mitigate voltage sags. However, in three-phase, three-wire systems, there is no dedicated path for the zero-sequence component of the grid current, resulting in voltage imbalances when unbalanced loads are present. Thus, DVRs designed for unbalanced loads must be re-engineered to ensure high-quality power delivery. Similar strategies for addressing power quality under uncertain grid conditions and load fluctuations have been explored in multi-agent energy systems, where flexibility and control robustness are achieved through advanced optimization techniques such as chance-constrained programming (CCP) [3,4].

To address power quality issues caused by asymmetrical loads in the grid system, a three-phase, four-leg inverter is proposed in [5] to generate a balanced grid voltage even under unbalanced load conditions. A key feature of the three-phase, four-leg inverter is the additional N-phase leg, which provides a dedicated path for zero-sequence currents. This additional leg allows for the adjustment of the neutral potential, addressing the limitations of traditional three-phase, three-leg inverters, where zero-sequence currents cannot be compensated, leading to voltage imbalance. By providing a clear path for zero-sequence currents, the three-phase, four-leg inverter ensures improved voltage balance and power quality in systems with unbalanced loads. Recent studies have emphasized the importance of advanced control strategies, such as adaptive control and virtual impedance methods, to further improve voltage compensation in dynamic and weak grid environments [6,7]. Additionally, the use of techniques like second-order generalized integrators (SOGIs) has

proven effective in filtering out disturbances and enhancing the control precision of grid-tied inverters under both balanced and unbalanced conditions [8].

The control loop of a three-phase, four-leg inverter typically includes a current control loop, a voltage control loop, sequence component separation, and a phase-locked loop (PLL). Control strategies can be implemented in either the dq frame or αβ frame. Proportional–integral (PI) controllers are commonly used for regulating voltage and current in the dq frame, while proportional resonant (PR) controllers are preferred for harmonic compensation in the αβ frame, as shown in previous studies [9,10]. In conditions where the system experiences unbalanced loads or grid voltages, it is crucial to separate the positive- and negative-sequence components of both current and voltage. This ensures the effective closed-loop control and synchronization of voltage to maintain system stability. To achieve this, the double second-order generalized integrator (DSOGI) is widely employed for orthogonal component reconstruction, allowing for the accurate calculation of positive- and negative-sequence components from sampled signals, as demonstrated by [11]. This method significantly improves the control system's performance in dynamic grid conditions, where voltage sags or distortions are common, as noted by [12] and further validated by [13] in their respective studies.

Traditional control methods, such as those applied in three-phase, four-leg inverters for uninterruptible power supplies (UPSs), have been widely used in various power electronics applications. However, when these methods are adapted for use in dynamic voltage restorers (DVRs), their effectiveness is often limited by the complexity of modern grid conditions, which include unbalanced voltages and fluctuating loads. One of the key challenges in DVR applications is achieving a rapid dynamic response to voltage sags, a critical requirement to ensure voltage stability for sensitive loads [14]. Although traditional double-loop control strategies—such as those incorporating negative-sequence component suppression—have been optimized to improve dynamic response, they often struggle to maintain performance under diverse operating conditions [15]. For example, control parameters that are fine-tuned for specific conditions may become suboptimal in the presence of varying load profiles or unbalanced grid voltages. Recent studies have highlighted these limitations, indicating that fixed-parameter control schemes may not provide sufficient flexibility in real-world applications. This has led to increased interest in adaptive and non-linear control strategies, which can adjust in real time to maintain robust performance across a wider range of scenarios [16,17].

Unlike traditional linear control methods, model predictive control (MPC) offers a superior dynamic response without relying on pulse-width modulation (PWM), which makes it particularly advantageous for inverter applications in dynamic and complex grid environments. Recent studies have demonstrated the effectiveness of MPC in grid-connected inverters, highlighting its ability to adapt to variable grid conditions and non-linearities without the complexities associated with conventional PWM schemes [18,19]. MPC can be broadly categorized into two types: finite-control-set (FCS) and continuous-control-set (CCS) MPC. FCS-MPC allows for direct control over switching states, resulting in faster dynamic response times, which are critical for effectively managing disturbances such as voltage sags and unbalanced loads [20]. FCS-MPC, being independent of PWM, operates with a variable switching frequency, making it suitable for applications less sensitive to switching frequency, while CCS-MPC leverages PWM to generate smooth control inputs, ideal for high-precision control demands [21]. CCS-MPC exhibits superior dynamic performance, particularly in scenarios where system parameters and load conditions frequently change, demonstrating higher fault tolerance. In contrast, FCS-MPC achieves lower total harmonic distortion (THD) under steady-state conditions [22].

Sliding mode control (SMC) offers robust performance in the face of parameter variations and external disturbances by forcing system states onto a predefined sliding surface [23]. While SMC excels in uncertain environments and is computationally simpler, it suffers from chattering, which can degrade performance [24]. MPC, particularly FCS-MPC, delivers precise control and flexibility in multi-variable systems but requires accurate mod-

els and greater computational resources. Ultimately, the choice between MPC and SMC hinges on specific application requirements: MPC is preferable for optimal performance under accurate modeling conditions, while SMC is advantageous in situations requiring simplicity and robustness against uncertainties [25].

FCS-MPC can regulate the voltage and current of the inverter without relying on a PWM loop, offering a significantly faster dynamic response compared to traditional linear controllers. In [26], FCS-MPC is applied to a three-phase, four-leg inverter to regulate grid current, further enhancing dynamic performance. However, this control method is primarily suited for L-filtered inverters. When applied to inverters with second-order filters, such as LC filters, the prediction model for state variables often lacks precision, limiting its effectiveness. To address this limitation, Ref. [27] proposed a model predictive voltage control scheme for LC-filtered three-phase, four-leg inverters, achieving constant voltage regulation without PWM. Despite this, the dynamic response remains constrained due to the use of CCS-MPC, which, while effective for steady-state control, does not provide the rapid dynamic response needed in scenarios like voltage sags or unbalanced loads. In contrast, Ref. [20] proposed an FCS-MPC method for LC-filtered inverters, demonstrating the fast and accurate regulation of three-phase voltages. However, its application to three-phase, four-leg inverters has yet to be fully verified.

Unlike traditional grid-connected inverters or voltage source inverters designed for passive loads, DVRs are connected in series with the system to compensate for load voltage, necessitating a much faster dynamic response. In DVR applications, the voltage reference must be calculated in real time within the controller. In [28], a DVR with an MPC-based three-phase NPC inverter was introduced, and they proposed a two-step indirect voltage prediction method to enhance control accuracy. Both symmetrical and asymmetrical voltage drops were analyzed and effectively compensated, further illustrating the potential of MPC in real-time voltage regulation for DVR applications.

The organization of this paper is as follows: Section 2 describes the topology of a DVR with a three-phase, four-leg inverter. Section 3 introduces the basic control loop of a DVR, focusing on sequence component separation and control strategies. In Section 4, the prediction model for an LC filter is established, and MPC for a three-phase, four-leg inverter is proposed to improve the dynamic response of a DVR. Section 5 presents the system's validation through MATLAB/Simulink simulations. Finally, conclusions are drawn in Section 6.

2. Description of the System

In this section, the topology of the three-phase, four-leg inverter used in the DVR system is presented. The fourth leg (N-phase) plays a critical role by providing a path for zero-sequence currents, allowing the system to effectively compensate for voltage imbalances in the presence of unbalanced loads. This makes the four-leg inverter superior to traditional three-leg inverters, especially under asymmetric load conditions. The inverter is connected in series with the power system, and its primary task is to maintain a balanced voltage supply to sensitive loads by dynamically compensating for voltage sags and fluctuations.

The topology of the three-phase, four-leg inverter is shown in Figure 1, and L is the filter inductor. v_x, u_{gx} and u_{lx} are the leg voltage, the grid voltage and the load voltage in phase $x(x = a, b, c)$. v_n is the voltage of phase n. u_x is the output voltage of the DVR in phase x. i_x and i_{gx} are the inductor current and output current of the DVR in phase x, respectively.

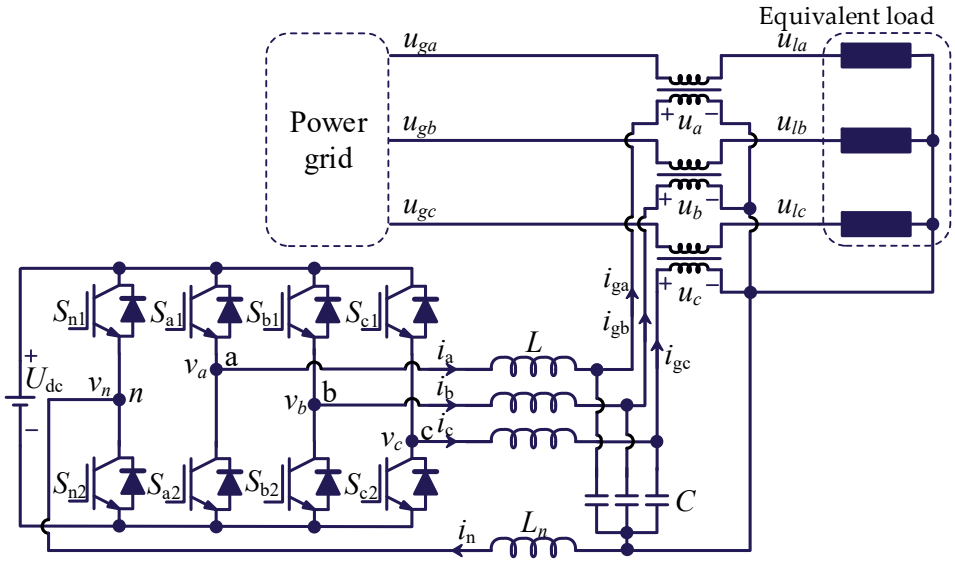

Figure 1. The topology of the three-phase, four-leg DVR.

The mathematical model of the inverter is derived in both the abc and αβγ coordinate systems. The abc frame is used for describing the three-phase voltages and currents in their natural form, while the αβγ frame provides a decoupled representation that simplifies the control of zero-sequence components.

According to Kirchhoff's law, the following equation can be derived as follows:

$$L\frac{\mathrm{d}}{\mathrm{dt}}\begin{bmatrix} i_a \\ i_b \\ i_c \end{bmatrix} = -L_n\frac{\mathrm{d}}{\mathrm{dt}}\begin{bmatrix} i_n \\ i_n \\ i_n \end{bmatrix} + \begin{bmatrix} v_{an} \\ v_{bn} \\ v_{cn} \end{bmatrix} - \begin{bmatrix} u_a \\ u_b \\ u_c \end{bmatrix} \tag{1}$$

$$\frac{\mathrm{d}}{\mathrm{dt}}\begin{bmatrix} u_a \\ u_b \\ u_c \end{bmatrix} = \frac{1}{C}\begin{bmatrix} i_a \\ i_b \\ i_c \end{bmatrix} - \frac{1}{C}\begin{bmatrix} i_{ga} \\ i_{gb} \\ i_{gc} \end{bmatrix} \tag{2}$$

$$i_a + i_b + i_c = i_n \tag{3}$$

where $v_{xn} = v_x - v_n (x = a, b, c)$.

From the Clark transform, the following equation can be derived as follows:

$$\begin{bmatrix} L\frac{\mathrm{d}}{\mathrm{dt}}i_\alpha \\ L\frac{\mathrm{d}}{\mathrm{dt}}i_\beta \\ (L+3L_n)\frac{\mathrm{d}}{\mathrm{dt}}i_\gamma \end{bmatrix} = \begin{bmatrix} v_{\alpha n} \\ v_{\beta n} \\ v_{\gamma n} \end{bmatrix} - \begin{bmatrix} u_\alpha \\ u_\beta \\ u_\gamma \end{bmatrix} \tag{4}$$

$$\frac{\mathrm{d}}{\mathrm{dt}}\begin{bmatrix} u_\alpha \\ u_\beta \\ u_\gamma \end{bmatrix} = \frac{1}{C}\begin{bmatrix} i_\alpha \\ i_\beta \\ i_\gamma \end{bmatrix} - \frac{1}{C}\begin{bmatrix} i_{g\alpha} \\ i_{g\beta} \\ i_{g\gamma} \end{bmatrix} \tag{5}$$

where the subscripts α, β, and γ represent the components of the αβ frame and the zero sequence, respectively.

This transformation provides a clear decoupling of the voltage components, with the αβ components representing the balanced part of the three-phase system, and the γ component handling the zero-sequence voltage. These decoupled components are particularly useful for model predictive control (MPC) as they allow for independent control over the different aspects of the inverter's output voltage.

The αβγ model is further employed in the development of the prediction model for the inverter, facilitating real-time voltage and current regulation. In Section 4, we will

demonstrate how this mathematical model is integrated into the MPC scheme to optimize the inverter's performance under varying grid conditions.

3. Control Loop Description

3.1. SOGI Structure

In order to separate the positive and negative components of the system, an SOGI is applied in the control loop, and the SOGI structure is shown in Figure 2. In Figure 2, ω_0 is the fundamental frequency, and k is the damping ratio.

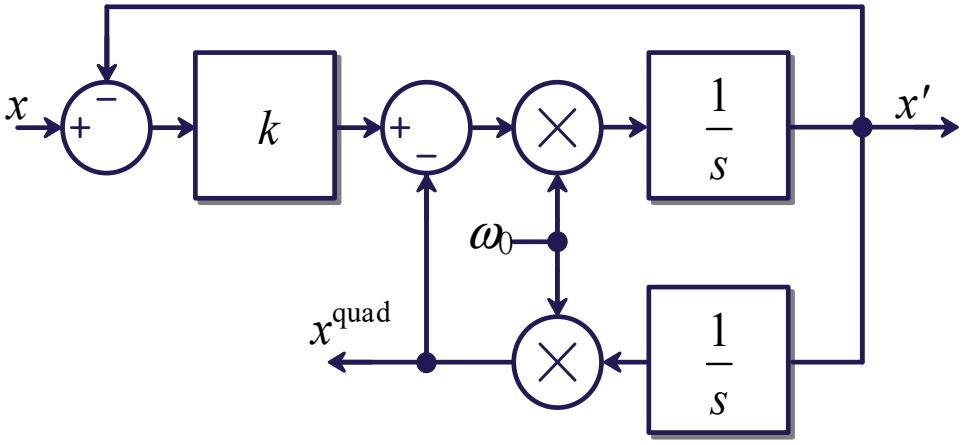

Figure 2. The SOGI structure.

The transfer function can be expressed as follows:

$$D(s) = \frac{x\prime(s)}{x(s)} = \frac{k\omega_0 s}{s^2 + k\omega_0 s + \omega_0^2} \tag{6}$$

$$Q(s) = \frac{x^{\text{quad}}(s)}{x(s)} = \frac{k\omega_0^2}{s^2 + k\omega_0 s + \omega_0^2} \tag{7}$$

The outputs of the SOGI x' and x^{quad} are orthogonal in the fundamental frequency.

3.2. Decoupling of Positive and Negative Sequences

As shown in Figure 2, the SOGI is used for the orthogonal reconstruction of the grid voltage in the αβ frame. Then, the positive and negative components in the αβ frame can be expressed as follows:

$$\begin{cases} x_\alpha^p = \frac{1}{2}(x'_\alpha - x_\beta^{\text{quad}}) \\ x_\alpha^n = \frac{1}{2}(x'_\alpha + x_\beta^{\text{quad}}) \end{cases} \tag{8}$$

$$\begin{cases} x_\beta^p = \frac{1}{2}(x'_\beta + x_\alpha^{\text{quad}}) \\ x_\beta^n = \frac{1}{2}(x'_\beta - x_\alpha^{\text{quad}}) \end{cases} \tag{9}$$

According to (8), the positive and negative components can be separated by the block diagram depicted in Figure 3. The vector relationship between the positive- and negative-sequence voltage components can be expressed as shown in Figure 4.

By combining the SOGI with (8) and (9), the voltage vector in the αβ frame can be decomposed into the positive-sequence voltage and the negative-sequence voltage, as shown in Figure 5.

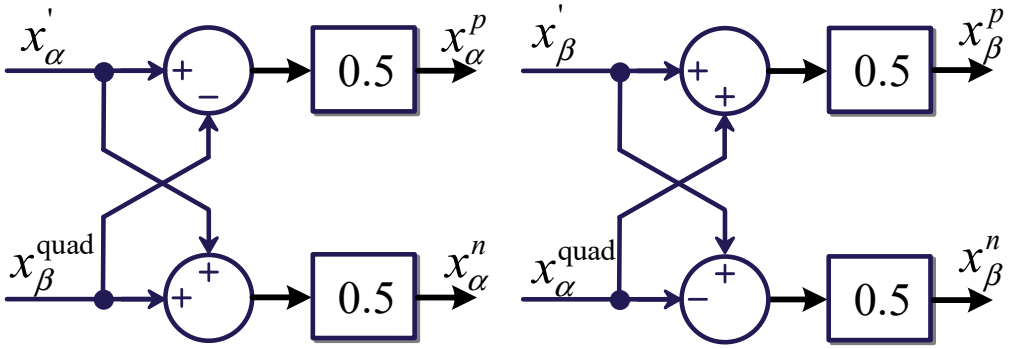

Figure 3. Extraction of positive- and negative-sequence components.

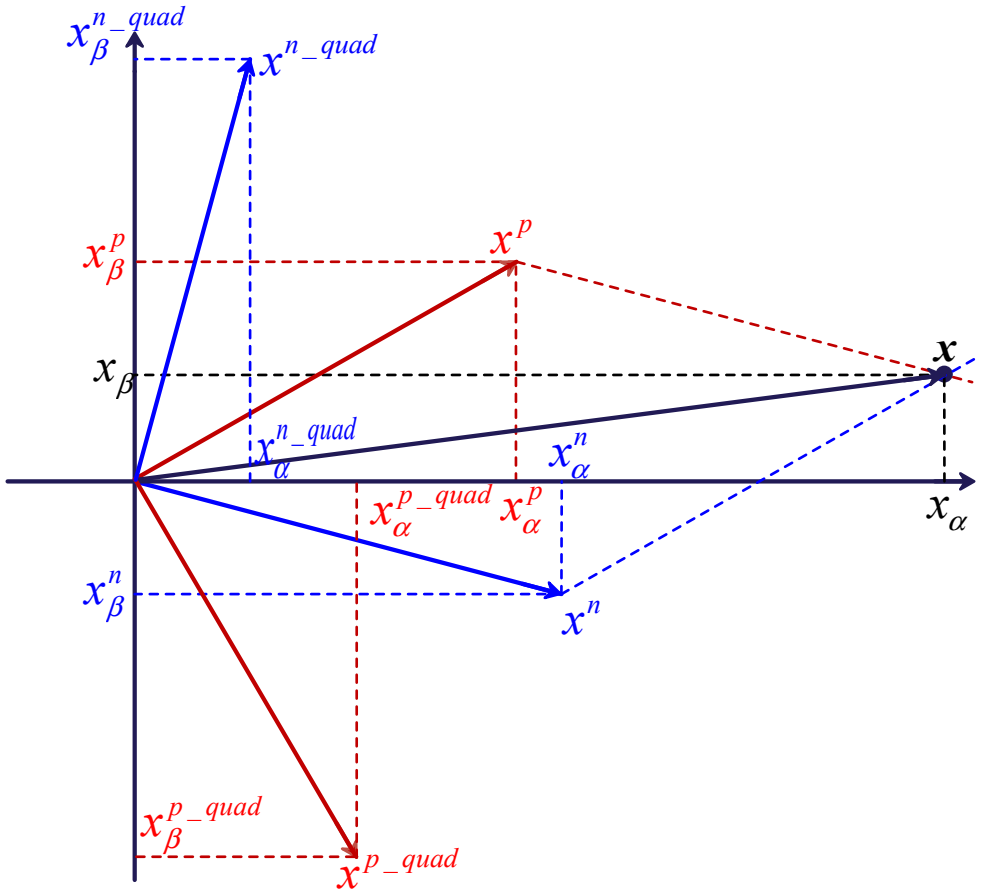

Figure 4. Voltage vector decoupling representation.

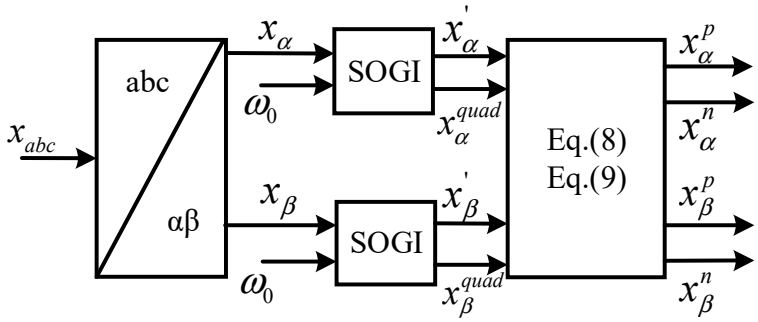

Figure 5. Block diagram of positive- and negative-sequence component separation.

The separated positive-sequence voltage will be applied for the voltage synchronization and double-loop control of the voltage and current. And the traditional control loop with a linear controller is illustrated in Figure 6. The superscripts p and n represent the positive- and negative-sequence components, respectively. The subscripts dq and dq_ref represent the components in dq frame, respectively.

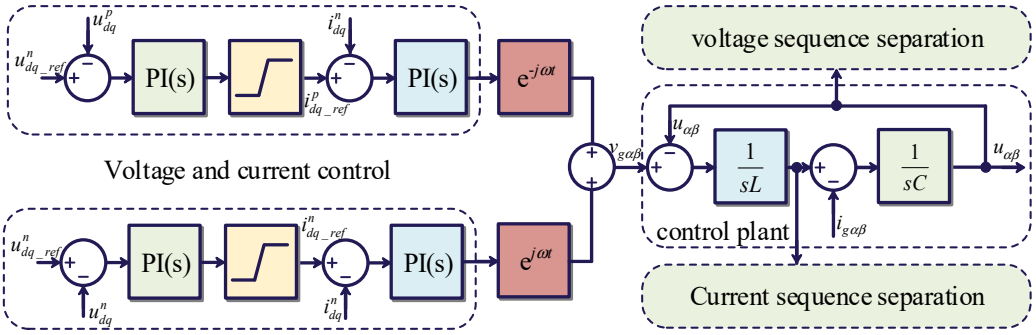

Figure 6. Block diagram of voltage control and current control of positive- and negative-sequence components.

It can be seen that the voltage and current sequence components should be separated by a DSOGI, which is a second-order filter, and the dynamic response will become slow due to this filter. The traditional method limits the dynamic response of the DVR under unbalanced grid conditions.

4. Model Predictive Control

Compared to traditional double-loop control, model predictive control can be used for voltage control without a current control loop or PWM loop, and the dynamic response is thereby improved dramatically. In MPC, the voltage and current can be predicted for the next interval by the established predictive model, and then the optimal voltage vector should be selected for the next control interval. Therefore, the predictive model, cost function, and voltage vector analysis are the main components of MPC.

4.1. Voltage Vector Analysis of Three-Phase, Four-Leg Inverter

It is assumed that S_a, S_b, S_c, and S_n represent the switching states of legs a(S_{a1},S_{a2}), b(S_{b1},S_{b2}), c (S_{c1},S_{c2}), and n (S_{n1},S_{n2}), respectively. In this topology, the switches in each leg must operate in a complementary manner. Specifically, a state of "1" indicates that the upper switch is ON and the lower switch is OFF, while a state of "0" indicates that the upper switch is OFF and the lower switch is ON. The four-leg, three-phase inverter has 16 possible switching configurations, which correspond to 16 voltage vectors.

The 16 switch configurations are (0,0,0,0), (0,0,1,0), (0,1,0,0), (0,1,1,0), (1,0,0,0), (1,0,0,1), (1,0,1,0), (1,1,0,0), (1,1,1,0), (0,0,0,1), (0,0,1,1), (0,1,0,1), (0,1,1,1), (1,0,1,1), (1,1,0,1), and (1,1,1,1). The 16 switching configurations are numbered sequentially to obtain the output voltages, v_{an}, v_{bn} and v_{cn}, of the three-phase, four-leg inverter. The output voltages, v_α, v_β and v_γ, of the inverter in the αβ frame for the different switching configurations are derived from the Clark transformation, as shown in Table 1.

Table 1. Effect of the combination of the inverter switch and inverter voltage.

Num	S_a	S_b	S_c	S_n	v_{an}	v_{bn}	v_{cn}	$v_{\alpha n}$	$v_{\beta n}$	v_γ
0	0	0	0	0	0	0	0	0	0	0
1	0	0	1	0	0	0	U_{dc}	$-U_{dc}/3$	$-U_{dc}/\sqrt{3}$	$U_{dc}/3$
2	0	1	0	0	0	U_{dc}	0	$-U_{dc}/3$	$U_{dc}/\sqrt{3}$	$U_{dc}/3$

Table 1. *Cont.*

Num	S_a	S_b	S_c	S_n	v_{an}	v_{bn}	v_{cn}	$v_{\alpha n}$	$v_{\beta n}$	v_γ
3	0	1	1	0	0	U_{dc}	U_{dc}	$-2U_{dc}/3$	0	$2U_{dc}/3$
4	1	0	0	0	U_{dc}	0	0	$2U_{dc}/3$	0	$U_{dc}/3$
5	1	0	1	0	U_{dc}	0	U_{dc}	$U_{dc}/3$	$-U_{dc}/\sqrt{3}$	$2U_{dc}/3$
6	1	1	0	0	U_{dc}	U_{dc}	0	$U_{dc}/3$	$U_{dc}/\sqrt{3}$	$2U_{dc}/3$
7	1	1	1	0	U_{dc}	U_{dc}	U_{dc}	0	0	U_{dc}
8	0	0	0	1	$-U_{dc}$	$-U_{dc}$	$-U_{dc}$	0	0	$-U_{dc}$
9	0	0	1	1	$-U_{dc}$	$-U_{dc}$	0	$-U_{dc}/3$	$-U_{dc}/\sqrt{3}$	$-2U_{dc}/3$
10	0	1	0	1	$-U_{dc}$	0	$-U_{dc}$	$-U_{dc}/3$	$U_{dc}/\sqrt{3}$	$-2U_{dc}/3$
11	0	1	1	1	$-U_{dc}$	0	0	$-2U_{dc}/3$	0	$-U_{dc}/3$
12	1	0	0	1	0	$-U_{dc}$	$-U_{dc}$	$2U_{dc}/3$	0	$-2U_{dc}/3$
13	1	0	1	1	0	$-U_{dc}$	0	$U_{dc}/3$	$-U_{dc}/\sqrt{3}$	$-U_{dc}/3$
14	1	1	0	1	0	0	$-U_{dc}$	$U_{dc}/3$	$U_{dc}/\sqrt{3}$	$-U_{dc}/3$
15	1	1	1	1	0	0	0	0	0	0

4.2. Discrete Model of Three-Phase, Four-Leg DVR

For simplicity, it is assumed that $u_{\alpha\beta} = u_\alpha + \mathrm{j}u_\beta$ and $i_{\alpha\beta} = i_\alpha + \mathrm{j}i_\beta$, $u_{\alpha\beta n} = u_{\alpha n} + \mathrm{j}u_{\beta n}$. This leads to the state space shown in Equation (10), where r is the parasitic resistor of the filter inductors.

$$\begin{bmatrix} \dot{i}_{\alpha\beta} \\ \dot{i}_\gamma \\ \dot{u}_{\alpha\beta} \\ \dot{u}_\gamma \end{bmatrix} = \begin{bmatrix} -\frac{r}{L} & 0 & -\frac{1}{L} & 0 \\ 0 & -\frac{r}{L+3L_n} & 0 & -\frac{1}{L+3L_n} \\ \frac{1}{C} & 0 & 0 & 0 \\ 0 & \frac{1}{C} & 0 & 0 \end{bmatrix} \begin{bmatrix} i_{\alpha\beta} \\ i_\gamma \\ u_{\alpha\beta} \\ u_\gamma \end{bmatrix} + \begin{bmatrix} \frac{1}{L} & 0 & 0 & 0 \\ 0 & \frac{1}{L+3L_n} & 0 & 0 \\ 0 & 0 & -\frac{1}{C} & 0 \\ 0 & 0 & 0 & -\frac{1}{C} \end{bmatrix} \begin{bmatrix} v_{\alpha\beta} \\ v_\gamma \\ i_{l\alpha\beta} \\ i_{l\gamma} \end{bmatrix} \tag{10}$$

Equation (10) can be simplified as follows:

$$\dot{x}(t) = Ax(t) + Bu(t) \tag{11}$$

where *x(t)* is the state variable of the system, and *u(t)* represents the voltage and current at the output of the inverter. When applying a zero-order holding input to a continuous time system in the form of the state space represented by Equation (11), a discrete state space model can be derived, as shown in (12).

$$x(k+1) = Gx(k) + Hu(k) \tag{12}$$

where

$$x(k) = \begin{bmatrix} i_{\alpha\beta}(k) \\ i_\gamma(k) \\ u_{\alpha\beta}(k) \\ u_\gamma(k) \end{bmatrix}, u(k) = \begin{bmatrix} v_{\alpha\beta}(k) \\ v_\gamma(k) \\ i_{g\alpha\beta}(k) \\ i_{g\gamma}(k) \end{bmatrix}, G = \mathrm{e}^{AT_s}, H = \int_0^{T_s} \mathrm{e}^{A(T_s-\tau)}Bd\tau \tag{13}$$

Furthermore, due to the time delay of the control interval, the two-step prediction method is used to predict the voltage and current. The predictive value of x at *(k + 2)* can be expressed as shown in (14) according to (12).

$$x(k+2) = Gx(k+1) + Hu(k+1) \tag{14}$$

where $x(k + 1)$ can be calculated by (7), in which $u(k)$ is a known value calculated by (8), and $v_{\alpha\beta}(k)$ and $v_\gamma(k)$ are predicted at the $(k - 1)$th instance.

Since the sampling frequency is much higher than the time constant of the inverter filter, it is assumed that the load currents, $i_{g\alpha\beta}$ and $i_{g\gamma}$, can be regarded as constants during one control cycle, and $v(k+1)$ is the desired value. Therefore, $u(k+1)$ in (14) can be expressed as follows:

$$u(k+1) = \begin{bmatrix} v_{\alpha\beta}(k+1) \\ v_{\gamma}(k+1) \\ i_{g\alpha\beta}(k+1) \\ i_{g\gamma}(k+1) \end{bmatrix} = \begin{bmatrix} v_{\alpha\beta}^{des}(k) \\ v_{\gamma}^{des}(k) \\ i_{g\alpha\beta}(k) \\ i_{g\gamma}(k) \end{bmatrix} \tag{15}$$

where $V_{\alpha\beta}^{des}(k)$ and $V_{\gamma}^{des}(k)$ are the desired voltage vectors predicted at the kth instance, which are derived from all 16 voltage vectors at the kth instance. Therefore, by substituting (15) and (12) into (14), the predictive voltage at the $k+2$ instance for the 16 voltage vectors listed in Table 1 can be calculated.

4.3. Estimation of the Reference

The Lagrange extrapolation method is a widely employed estimation approach in model predictive control. It leverages polynomial functions constructed from known control variables to estimate other unknown variables or the control variables for the subsequent time step. This method enables the construction of an nnnth-order polynomial based on sampled values, facilitating prediction for the next time step and achieving anticipatory estimation. It is necessary to estimate the reference voltage at the $k+2$ step, and the Lagrange extrapolation method is used for estimation in this paper.

$u_{ref}(k)$ is the reference value of the compensation voltage generated in real time by the DVR detection unit at time k. After the decoupling of the SOGI, the positive-sequence voltage vector expression is obtained as shown in (16).

$$u_{ref-\alpha\beta}^{+}(k) = u_{ref-\alpha}^{+}(k) + \mathrm{j}u_{ref-\beta}^{+}(k) = A^{+}\mathrm{e}^{\mathrm{j}\theta^{+}(k)} \tag{16}$$

The positive-sequence voltage reference to be compensated by the DVR at the $k+2$ instance is

$$u_{ref-\alpha\beta}^{+}(k+2) = 6u_{ref-\alpha\beta}^{+}(k) - 8u_{ref-\alpha\beta}^{+}(k-1) + 3u_{ref-\alpha\beta}^{+}(k-2) \tag{17}$$

Similarly, the negative-sequence voltage reference to be compensated by the DVR at the $k+2$ instance can be obtained as follows:

$$u_{ref-\alpha\beta}^{-}(k+2) = 6u_{ref-\alpha\beta}^{-}(k) - 8u_{ref-\alpha\beta}^{-}(k-1) + 3u_{ref-\alpha\beta}^{-}(k-2) \tag{18}$$

Combining Equations (17) and (18) gives

$$\begin{aligned} u_{ref-\alpha\beta}(k+2) &= \left[u_{ref-\alpha}^{+}(k+2) + u_{ref-\alpha}^{-}(k+2)\right] + \mathrm{j}\left[u_{ref-\beta}^{+}(k+2) + u_{ref-\beta}^{-}(k+2)\right] \\ &= u_{ref-\alpha\beta}^{+}(k+2) + u_{ref-\alpha\beta}^{-}(k+2) = u_{ref-\alpha}(k+2) + \mathrm{j}u_{ref-\beta}(k+2) \end{aligned} \tag{19}$$

The estimated zero-sequence voltage reference is

$$u_{ref-\gamma}(k+2) = 6u_{ref-\gamma}(k) - 8u_{ref-\gamma}(k-1) + 3u_{ref-\gamma}(k-2) \tag{20}$$

4.4. Establishment of Cost Function

The cost function of the system is established by the predicted voltage output and the reference of the compensation voltage, and the cost function can be written as

$$\begin{aligned} J &= \left[u_{ref-\alpha}(k+2) - u_{pre-\alpha}(k+2)\right]^2 + \left[u_{ref-\beta}(k+2) - u_{pre-\beta}(k+2)\right]^2 \\ &+ \left[u_{ref-\gamma}(k+2) - u_{pre-\gamma}(k+2)\right]^2 \end{aligned} \tag{21}$$

It is defined that i_{next} is the optimal switching configuration applied at the instance $k + 1$.

$$\begin{cases} J_i = \min J \\ i_{next} = i \end{cases} \tag{22}$$

In summary, a control cycle first executes the optimal switching configuration at that moment and then samples and makes predictions to obtain the optimal switching configuration for the next control cycle, and a control cycle flowchart is shown in Figure 7.

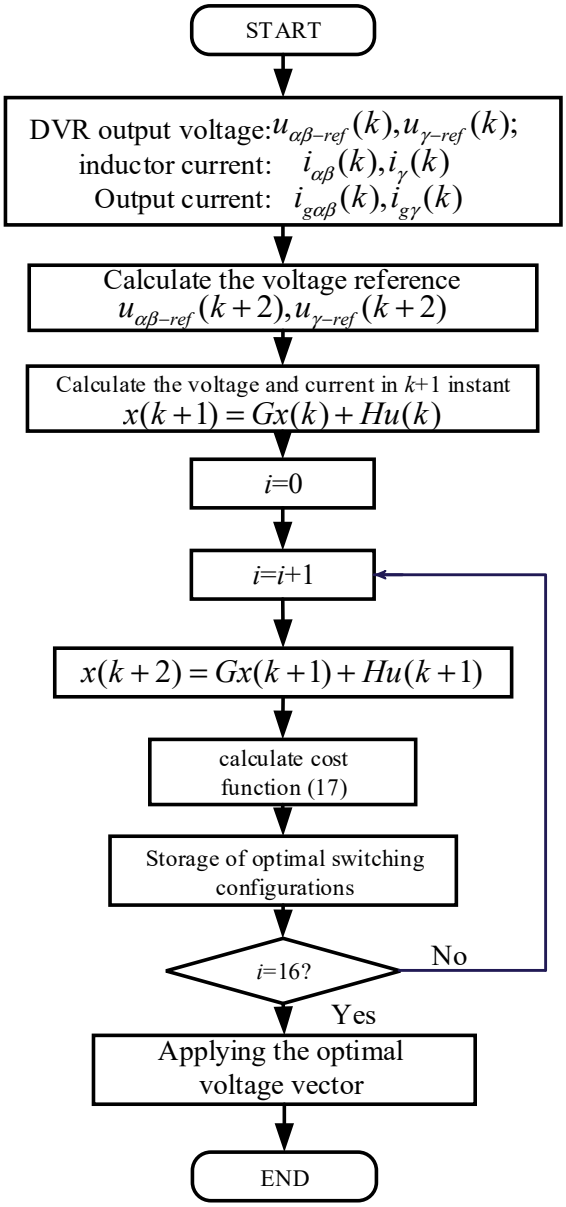

Figure 7. Flowchart of MPC with four-leg, three-phase inverter for DVR.

5. Simulation Results

This section presents the results from the MATLAB/Simulink simulations conducted to validate the performance of the proposed finite-control-set model predictive control (FCS-MPC) strategy for the three-phase, four-leg dynamic voltage restorer (DVR). The simulations were configured with a DC power supply, a transformer, a three-phase, four-leg inverter, and an inductive–capacitive filter under various load conditions.

5.1. Setup

The simulation setup in MATLAB/Simulink includes a DC voltage source of 600 V, an AC voltage source of 220 V (50 Hz), and asymmetrical load configurations. The simulation aimed to explore the DVR's response under varying voltage sag depths, different load types, and harmonic distortions. The parameters for the MATLAB/Simulink simulations are detailed in Table 2.

Table 2. Parameters for simulations.

Parameter	Values
DC voltage source	800 V
RMS value of rated AC voltage source	220 V
Frequency of AC voltage sources	50 Hz
Equivalent resistance of filter inductor	0.2 Ω
Filter inductors	1 mH
Filter inductance in N-phase	1 mH
Filter capacitors	500 μF
Switching frequency	5×10^{-5} s
Transformation ratio	1:1

5.2. Overview of Results

This section presents an overview of the MATLAB/Simulink simulation results, evaluating the performance of the proposed FCS-MPC strategy for the DVR under various voltage disturbances and load conditions. The simulations cover symmetrical and asymmetrical voltage sags, as well as harmonic disturbances with non-linear loads.

5.2.1. Symmetrical Voltage Sag

Symmetrical voltage sags of 30%, 60% and 90% were introduced in the simulation between 0.3 and 0.4 s to evaluate the DVR's response. During each sag event, the DVR was configured to restore the load voltage and maintain stability across these varying levels of disturbance, allowing for the assessment of the FCS-MPC strategy's performance under different sag conditions. As shown in Figures 8–10, symmetrical voltage sags of 30%, 60%, and 90% were introduced in the simulation, respectively. Figure 8 illustrates the DVR's response to a 30% voltage sag, Figure 9 shows the response to a 60% voltage sag, and Figure 10 depicts the response to a 90% voltage sag.

During the 30%, 60% and 90% symmetrical voltage sags, the DVR successfully restored the load voltage to a value close to the rated levels, within 1 millisecond, demonstrating rapid compensation and a stable response across all sag depths.

5.2.2. Asymmetrical Voltage Sag

An asymmetrical voltage sag was introduced with a 70% voltage drop in phase A, a 50% drop in phase B and an 80% drop in phase C. The DVR responded within 1 millisecond, restoring the load voltage to levels close to the rated value with minimal overshoot and oscillation. The simulation results for this scenario are shown in Figure 11.

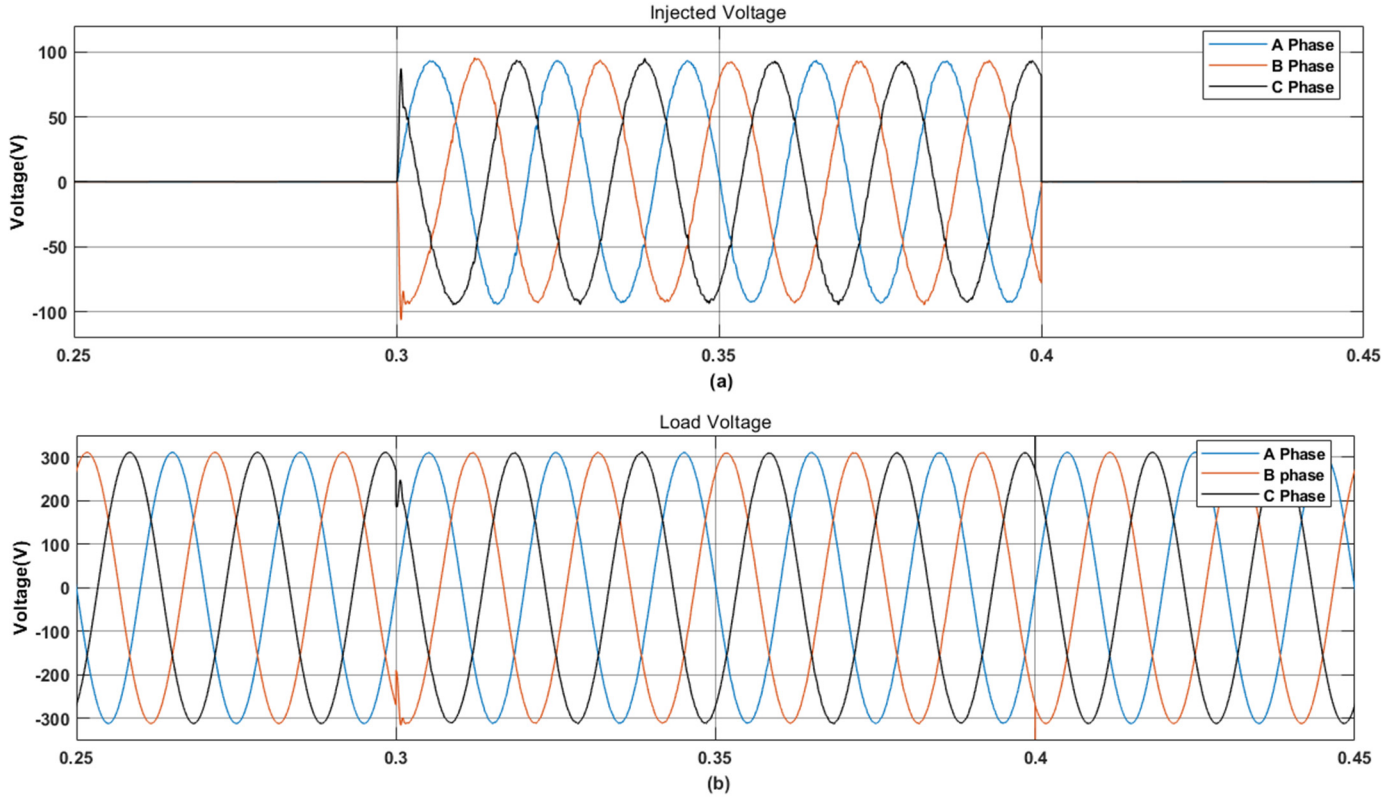

Figure 8. Simulated symmetrical voltage sag at 30%. (**a**) Injected Voltage. (**b**) Load Voltage.

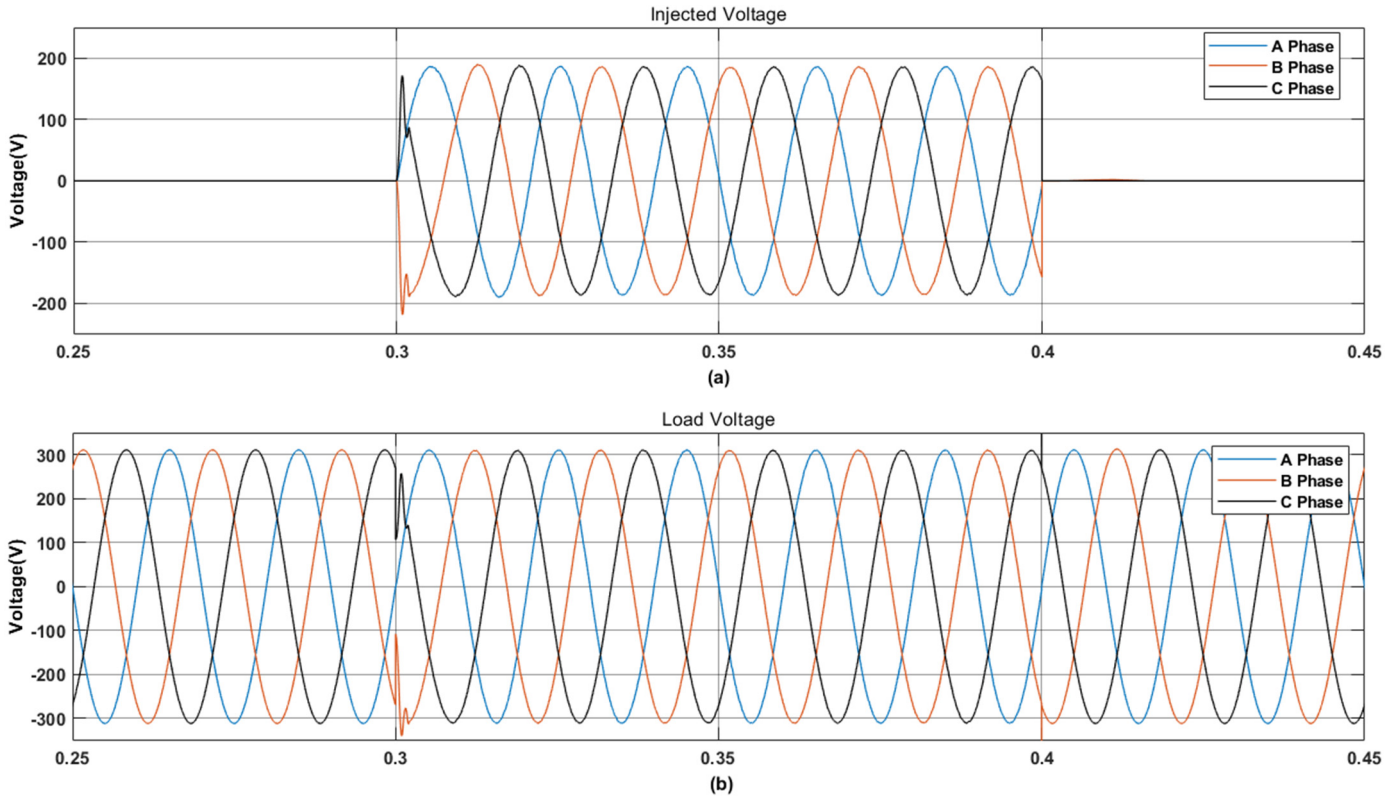

Figure 9. Simulated symmetrical voltage sag at 60%. (**a**) Injected Voltage. (**b**) Load Voltage.

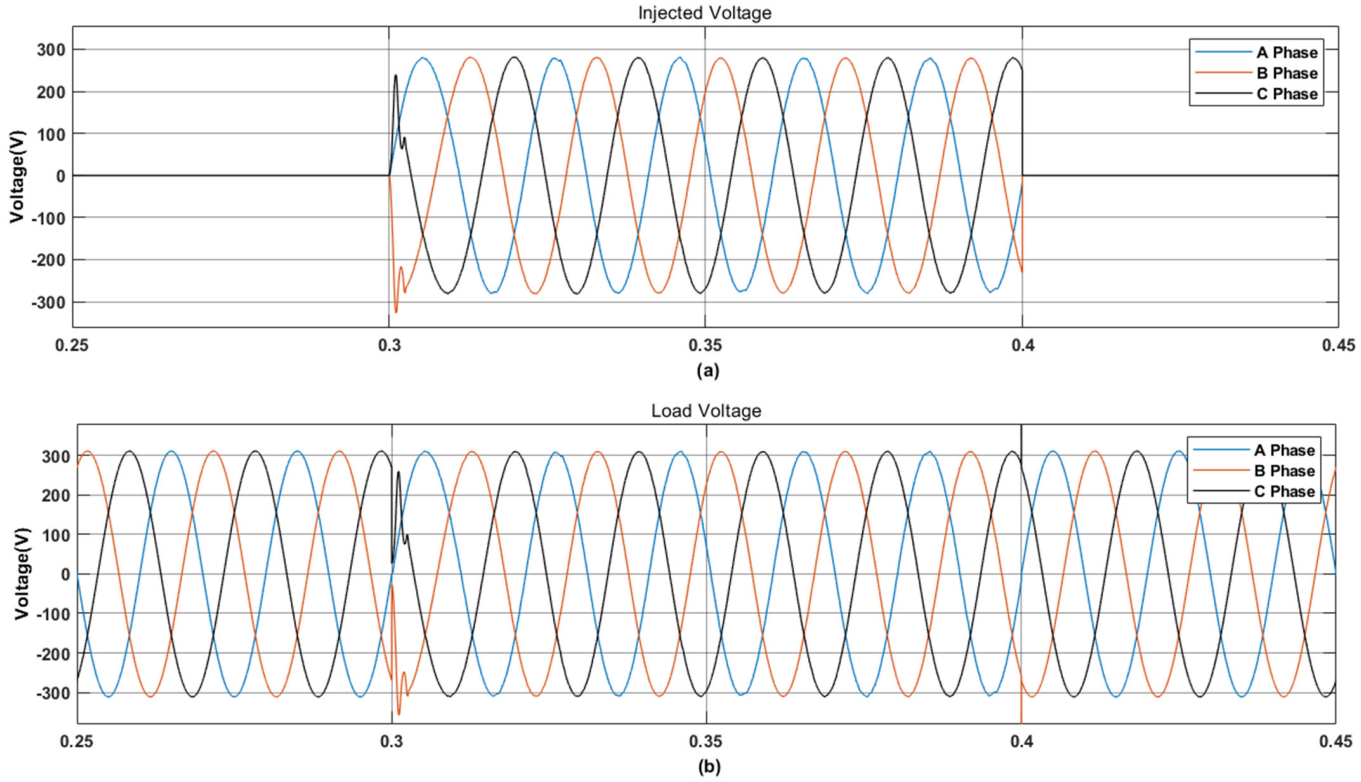

Figure 10. Simulated symmetrical voltage sag at 90%. (**a**) Injected Voltage. (**b**) Load Voltage.

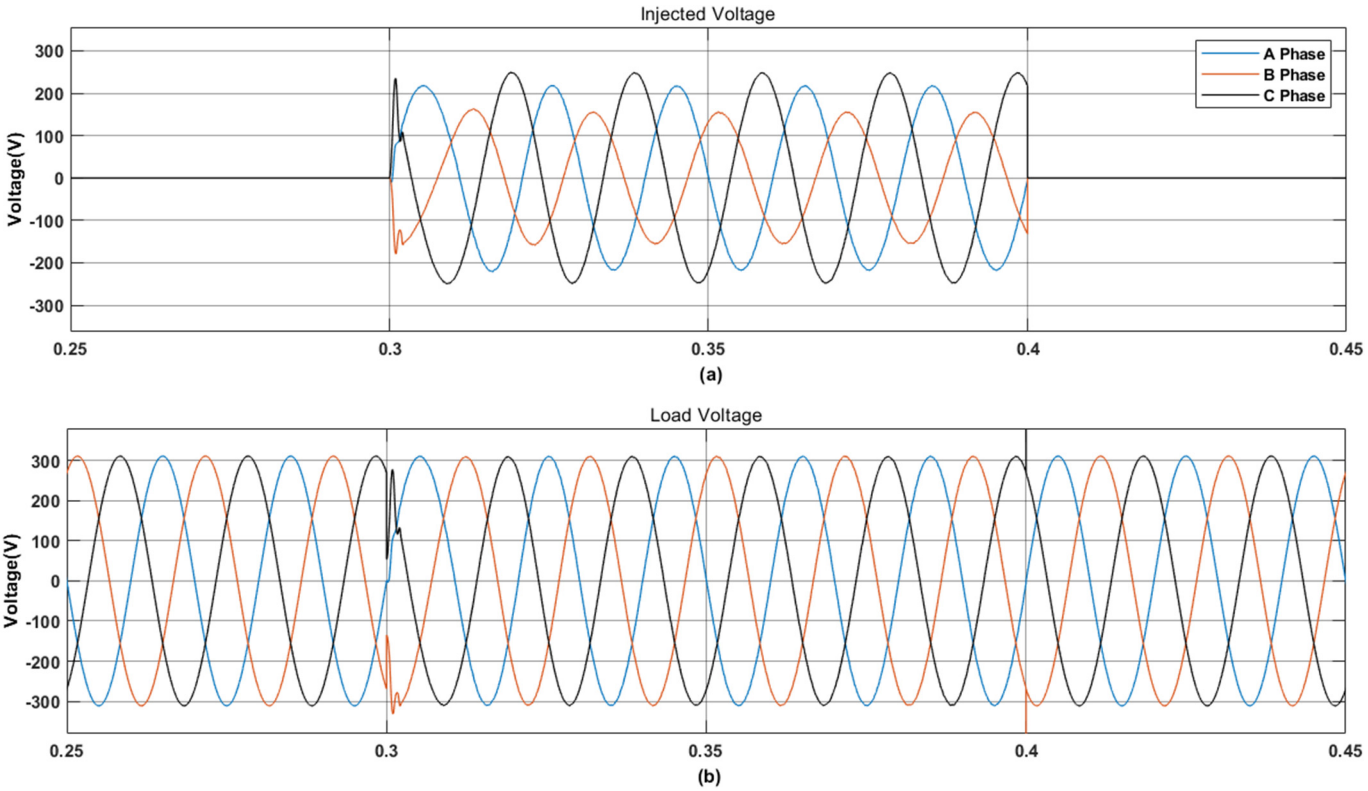

Figure 11. Simulated asymmetrical voltage sag with 70% drop in phase A, 50% in phase B and 80% in phase C. (**a**) Injected Voltage. (**b**) Load Voltage.

This result indicates the DVR's capability to manage unbalanced load conditions.

5.2.3. Voltage Sag Compensation for Non-Linear Loads

To evaluate voltage fluctuation compensation under non-linear load conditions, a three-phase, rectifier-based non-linear load with a resistance of 20 Ω and an inductance of 10 mH was used. Various levels of voltage sags were introduced into the grid, and the DVR's impact on the load-side voltage was analyzed. Voltage sags of 60% and 90% of the rated grid voltage were introduced. The simulation results for the 60% voltage sag are shown in Figure 12, and those for the 90% voltage sag are shown in Figure 13.

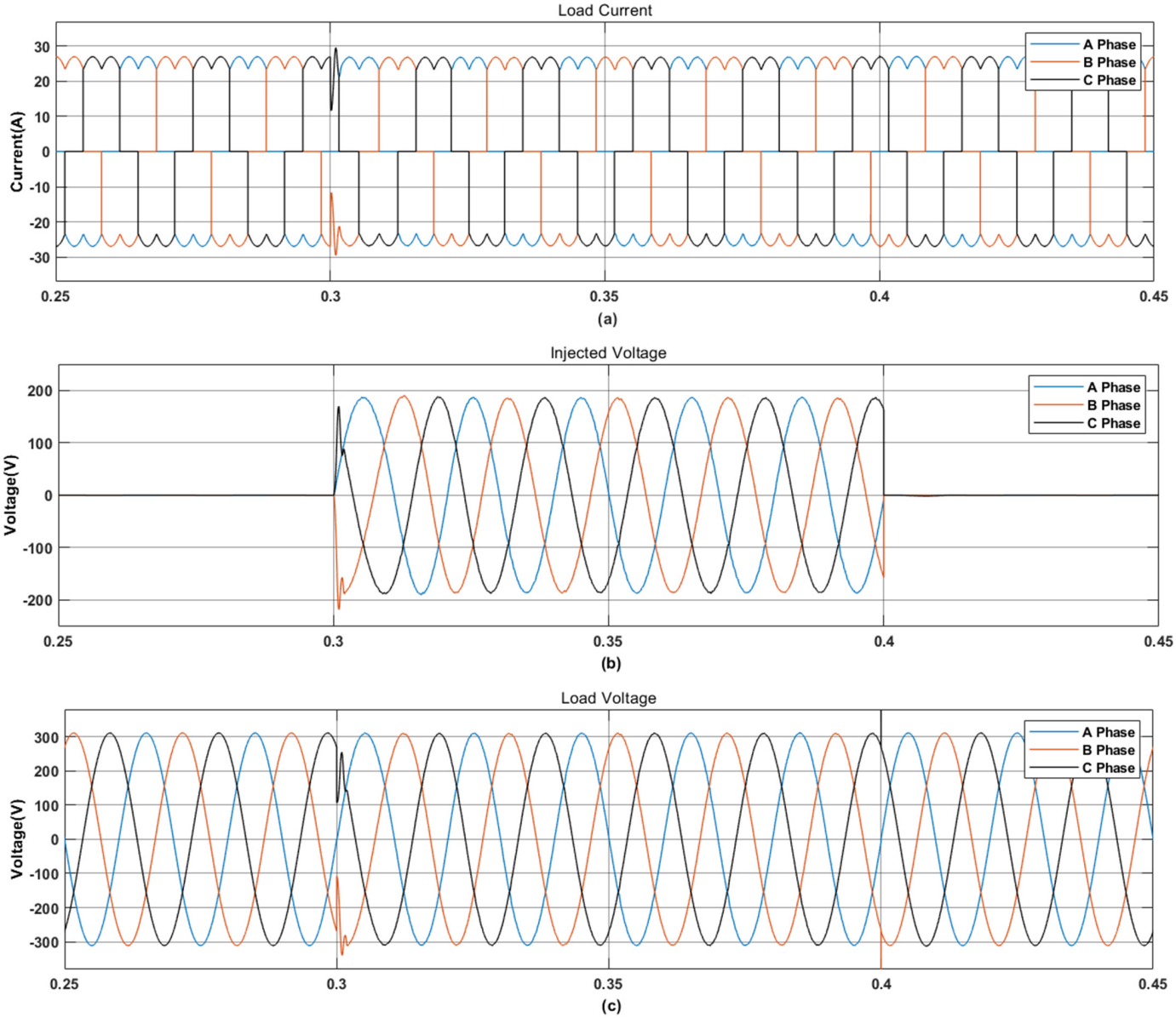

Figure 12. Voltage recovery under non-linear load with rectifier-based configuration (60% voltage sag). (**a**) Load Current. (**b**) Injected Voltage. (**c**) Load Voltage.

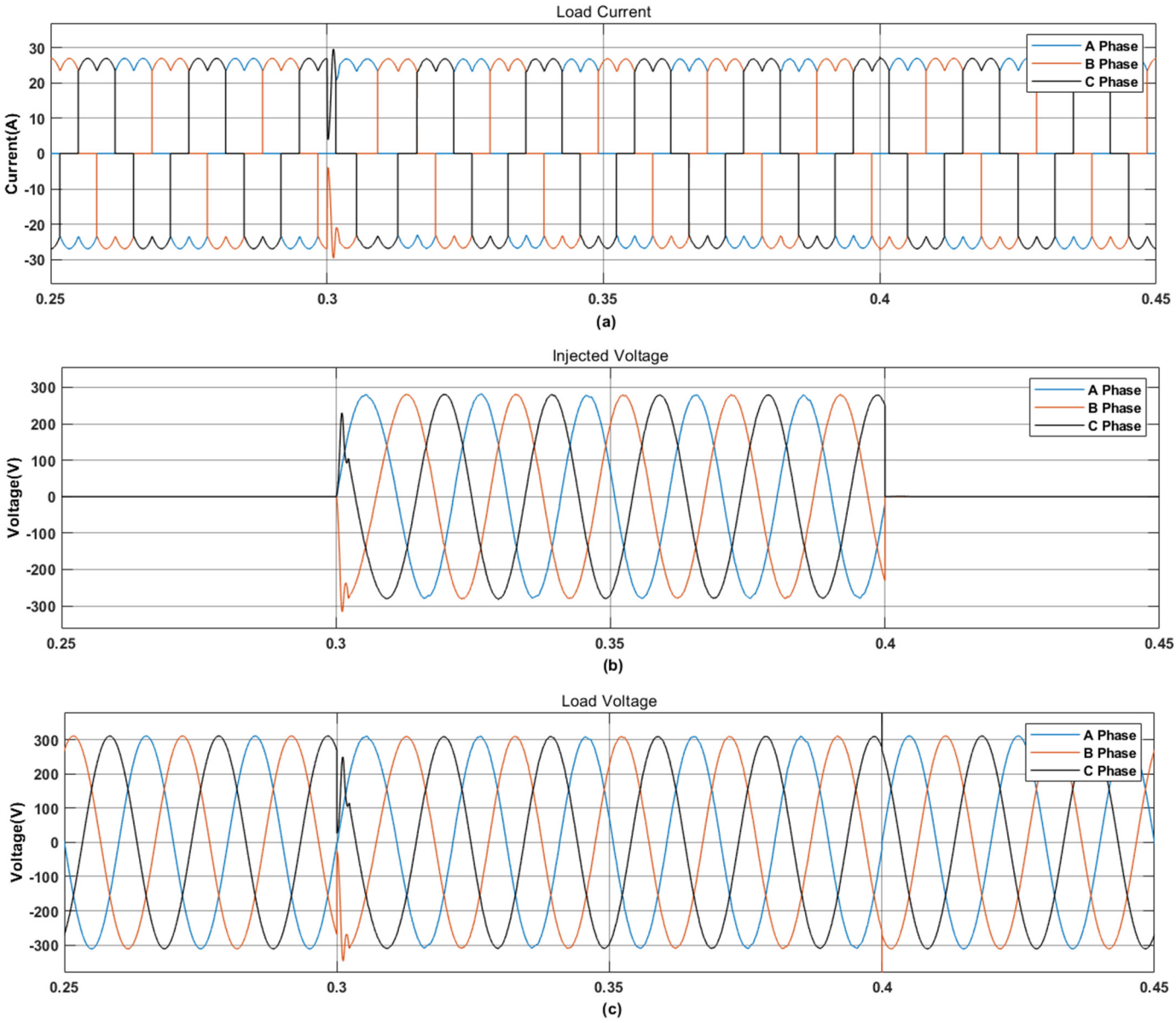

Figure 13. Voltage recovery under non-linear load with rectifier-based configuration (90% voltage sag). (**a**) Load Current. (**b**) Injected Voltage. (**c**) Load Voltage.

The simulation results show that the DVR quickly responds to the sag, restoring the load voltage to values close to the rated levels.

5.2.4. Harmonic Mitigation Performance Analysis

This section evaluates the DVR's harmonic mitigation performance under non-linear loads with harmonic disturbances. Two scenarios are tested: in the first scenario, the third, fifth, and seventh harmonics are introduced with amplitudes of 10%, 10% and 5% of the fundamental voltage, respectively. In the second scenario, the harmonics are set to 15% for the third, 10% for the fifth, and 5% for the seventh. These configurations allow for assessing the DVR's ability to suppress harmonics of varying magnitudes.

The DVR's harmonic mitigation performance under scenario 1, with the third, fifth, and seventh harmonics set to 10%, 10%, and 5% of the fundamental voltage, is shown in Figure 14a–c.

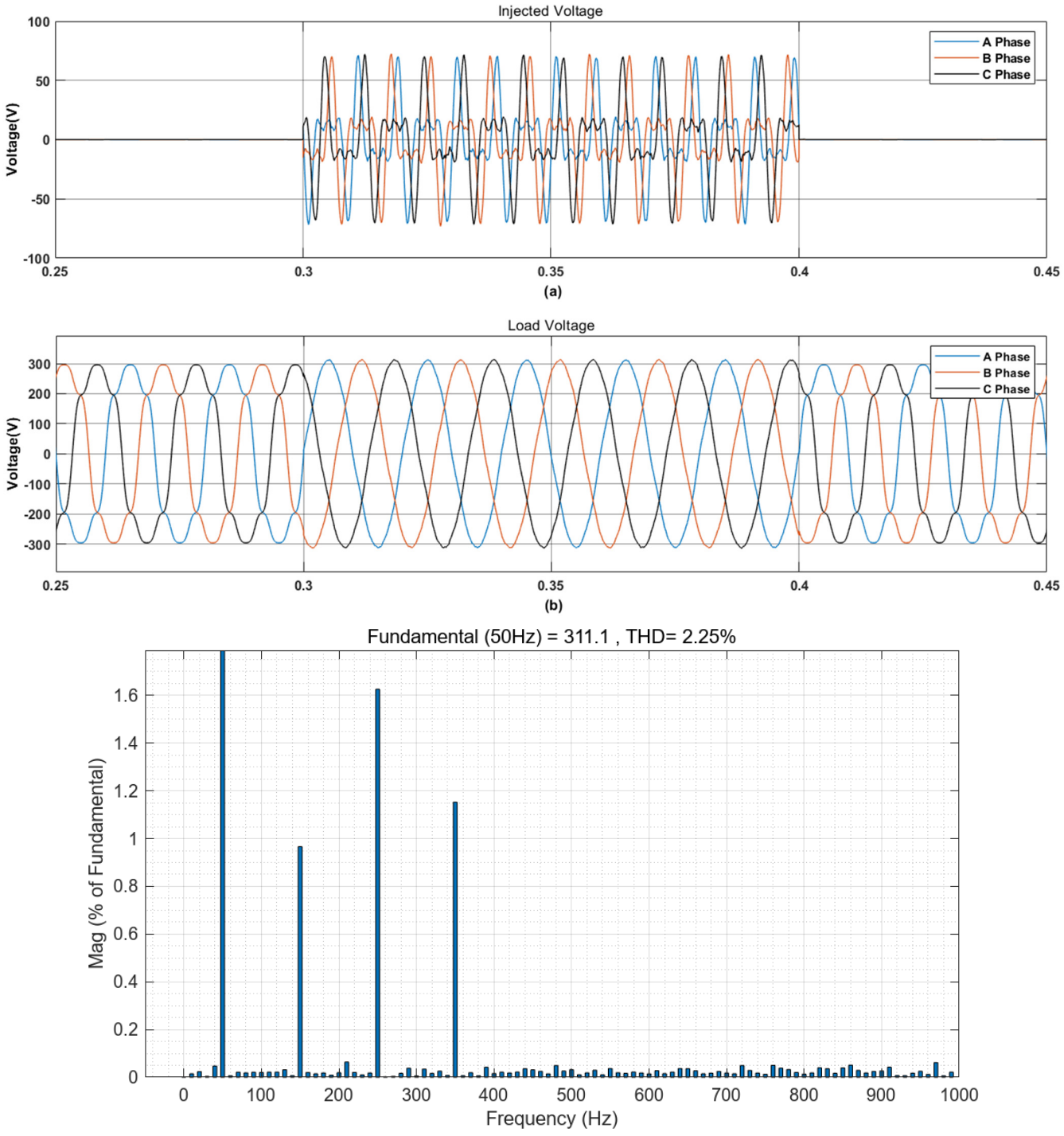

Figure 14. Harmonic distortion spectrum before and after DVR compensation (scenario 1: 3rd, 5th and 7th harmonics at 10%, 10% and 5%). (**a**) Injected Voltage. (**b**) Load Voltage. (**c**) Harmonic distortion spectrum after compensation.

The DVR's harmonic mitigation performance under scenario 2, with the third, fifth, and seventh harmonics set to 15%, 10%, and 5% of the fundamental voltage, is shown in Figure 15a–c.

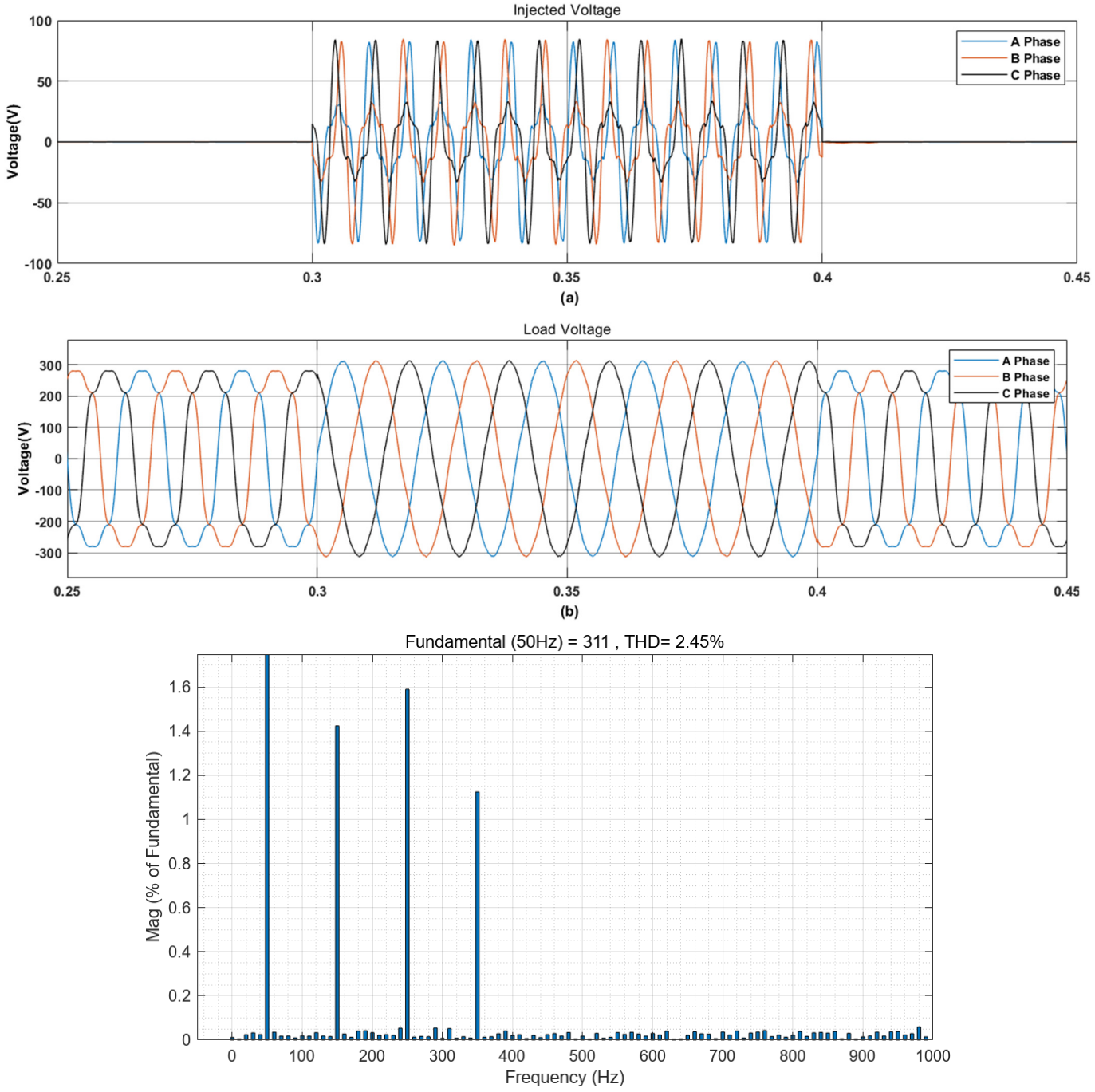

Figure 15. Harmonic distortion spectrum before and after DVR compensation (scenario 2: 3rd, 5th and 7th harmonics at 15%, 10% and 5%). (**a**) Injected Voltage. (**b**) Load Voltage. (**c**) Harmonic distortion spectrum after compensation.

The harmonic spectrum and total harmonic distortion (THD) values before and after compensation demonstrate the DVR's effectiveness in reducing THD, thereby ensuring stable power quality on the load side.

5.3. Discussion and Analysis

The MATLAB/Simulink simulation results validate the proposed FCS-MPC strategy's efficacy in managing various voltage sag scenarios. The DVR consistently demonstrated

quick voltage recovery across symmetrical and asymmetrical conditions. Notably, the system maintained stability even under non-linear load conditions, where traditional DVRs might struggle.

The addition of harmonic distortions provided further insights into the DVR's performance. The combination of FCS-MPC and SOGI filtering proved effective in mitigating harmonics, ensuring a clean voltage output.

6. Conclusions

This paper presents a model predictive control (MPC) method for a three-phase, four-leg dynamic voltage restorer (DVR). The MATLAB/Simulink simulation results demonstrate that the proposed finite-control-set MPC (FCS-MPC) method significantly enhances the DVR's dynamic response to various voltage disturbances. The simulation results under different load and harmonic conditions confirm the robustness and effectiveness of the control strategy, showing consistent and reliable performance across symmetrical and asymmetrical voltage sags as well as harmonic distortion scenarios.

The MATLAB/Simulink simulation was conducted to verify the correctness of the proposed MPC method:

(1) Compared to a traditional DVR with a three-phase, three-leg inverter, a DVR with a three-phase, four-leg inverter can be used to compensate for the unbalanced voltage and load effectively.
(2) The MPC method for a three-phase, four-leg inverter can enhance its dynamic response without requiring a double control loop or PWM.
(3) The control parameter is easily designed in the MPC method. Positive and negative control loops are not necessary in MPC.

Author Contributions: Conceptualization, D.L. and X.L.; methodology, D.L.; software, D.L.; validation, H.Z. and S.D.; formal analysis, H.Z.; investigation, D.L.; resources, X.L.; data curation, S.D.; writing—original draft preparation, D.L.; writing—review and editing, X.L. and H.Z.; visualization, D.L.; supervision, X.L.; project administration, X.L.; funding acquisition, S.D. All authors have read and agreed to the published version of the manuscript.

Funding: This work was supported in part by the Science and Technology Project of the China Southern Power Grid Corporation (090000KC23020073).

Data Availability Statement: The original contributions presented in the study are included in the article, and further inquiries can be directed to the corresponding author.

Conflicts of Interest: Authors Huaying Zhang, Xiaorui Liang and Shicong Deng was employed by the company China Southern Power Grid. The remaining authors declare that the research was conducted in the absence of any commercial or financial relationships that could be construed as a potential conflict of interest.

References

1. Arias-Guzman, S.; Ruiz-Guzman, O.A.; Garcia-Arias, L.F.; Jaramillo-Gonzales, M.; Cardona-Orozco, P.D.; Ustariz-Farfan, A.J.; Cano-Plata, E.A.; Salazar-Jimenez, A.F. Analysis of voltage sag severity case study in an industrial circuit. In Proceedings of the 2015 IEEE Industry Applications Society Annual Meeting, Addison, TX, USA, 18–22 October 2015; pp. 1–6.
2. Aldi, P.; Shrigiri, S.; Smita, K. Study of Topologies, Power Converters, and Control Techniques for the Dynamic Voltage Restorer (DVR). In Proceedings of the 2023 International Conference on Integrated Intelligence and Communication Systems (ICIICS), Kalaburagi, India, 24–25 November 2023; pp. 1–7.
3. Zhang, H.; Li, Z.; Xue, Y.; Chang, X.; Su, J.; Wang, P.; Guo, Q.; Sun, H. A Stochastic Bi-level Optimal Allocation Approach of Intelligent Buildings Considering Energy Storage Sharing Services. *IEEE Trans. Consum. Electron.* **2024**. [CrossRef]
4. Ding, B.; Li, Z.; Li, Z.; Xue, Y.; Chang, X.; Su, J.; Jin, X.; Sun, H. A CCP-based distributed cooperative operation strategy for multi-agent energy systems integrated with wind, solar, and buildings. *Appl. Energy* **2024**, *365*, 123275. [CrossRef]
5. Kim, J.-H.; Sul, S.-K. A carrier-based PWM method for three-phase four-leg voltage source converters. *IEEE Trans. Power Electron.* **2004**, *19*, 66–75.
6. Wang, H.; Lei, H.; Pei, X. Research on an Adaptive Compound Control Strategy of a Hybrid Compensation System. *Processes* **2023**, *11*, 2109. [CrossRef]

7. Kumar, A.; Kumar, P. Efficient controller of DSTATCOM based on combination of Adaline and SOGI-FLL for power quality improvement. *Int. J. Syst. Assur. Eng. Manag.* **2023**, *14*, 1543–1566. [CrossRef]
8. Golestan, S.; Guerrero, J.M.; Vasquez, J.C.; Abusorrah, A.M.; Al-Turki, Y. Modeling, Tuning, and Performance Comparison of Second-Order-Generalized-Integrator-Based FLLs. *IEEE Trans. Power Electron.* **2018**, *33*, 10229–10239. [CrossRef]
9. Qing, H.; Zhang, C.; Chai, X.; He, H.; Wang, X. Research on grid-connected harmonic current suppression of three-phase four-wire energy storage inverters. *J. Power Electron.* **2023**, *23*, 972–983. [CrossRef]
10. Quan, X. Improved Dynamic Response Design for Proportional Resonant Control Applied to Three-Phase Grid-Forming Inverter. *IEEE Trans. Ind. Electron.* **2021**, *68*, 9919–9930. [CrossRef]
11. Peng, L.; Fu, Z.; Xiao, T.; Qian, Y.; Zhao, W.; Zhang, C. An Improved Dual Second-Order Generalized Integrator Phased-Locked Loop Strategy for an Inverter of Flexible High-Voltage Direct Current Transmission Systems under Nonideal Grid Conditions. *Processes* **2023**, *11*, 2634. [CrossRef]
12. Xu, C.; Hou, S.; Chen, J. An Improved High Bandwidth DSOGI-PLL and its Optimized Digital Implementation. In Proceedings of the 2022 IEEE International Power Electronics and Application Conference and Exposition (PEAC), Guangzhou, China, 4–7 November 2022; pp. 1063–1068.
13. Ranjan, A.; Kewat, S.; Singh, B. DSOGI-PLL Based Solar Grid Interfaced System for Alleviating Power Quality Problems. In Proceedings of the 2019 National Power Electronics Conference (NPEC), Tiruchirappalli, India, 13–15 December 2019; pp. 1–6.
14. Srivastava, A.; Bajpai, R.S. Comparative Analysis of PI & MPC Controllers for Dynamic Voltage Restorer using Wind Energy Conversion System. In Proceedings of the 2021 4th Biennial International Conference on Nascent Technologies in Engineering (ICNTE), Navi Mumbai, India, 15–16 January 2021; pp. 1–6.
15. Rauf, A.M.; Khadkikar, V. An Enhanced Voltage Sag Compensation Scheme for Dynamic Voltage Restorer. *IEEE Trans. Ind. Electron.* **2015**, *62*, 2683–2692. [CrossRef]
16. Mohamed, A. A finite control set model predictive control scheme for single-phase grid-connected inverters. *Renew. Sustain. Energy Rev.* **2021**, *135*, 110131.
17. Zhu, Y.; Wen, H.; Yang, Y.; Mao, J.; Wang, P.; Huang, W.; Rodriguez, J. Decoupled Continuous Control Set Model Predictive Control for T-Type Three-Phase Four-Leg Three-Level Inverters Driving Constant Power Loads. *IEEE Trans. Power Electron.* **2024**, *39*, 7002–7015. [CrossRef]
18. Zaid, S.A.; Bakeer, A.; Albalawi, H.; Alatwi, A.M.; Abdeldaim, H.; Manqarah, B. Model-Free Predictive Current Control of a 3-φ Grid-Connected Neutral-Point-Clamped Transformerless Inverter. *Energies* **2023**, *16*, 3141. [CrossRef]
19. Hu, J.; Zhu, J.; Dorrell, D.G. Model Predictive Control of Grid-Connected Inverters for PV Systems with Flexible Power Regulation and Switching Frequency Reduction. *IEEE Trans. Ind. Appl.* **2015**, *51*, 587–594. [CrossRef]
20. Andang, A.; Pamungkas, T.A.; Busaeri, N.; Hartati, R.S.; Manuaba, I.B.G.; Kumara, I.N.S. Three-phase Four-leg Inverter LC Filter Using FCS MPC. In Proceedings of the International Conference on Smart-Green Technology in Electrical and Information Systems (ICSGTEIS), Sanur, Indonesia, 28–30 October 2021.
21. Ahmed, A.A.; Koh, B.K.; Lee, Y.I. A Comparison of Finite Control Set and Continuous Control Set Model Predictive Control Schemes for Speed Control of Induction Motors. *IEEE Trans. Ind. Inform.* **2017**, *14*, 1334–1346. [CrossRef]
22. Yang, J.; Liu, Y.; Yan, R. A Comparison of Finite Control Set and Continuous Control Set Model Predictive Control Schemes for Model Parameter Mismatch in Three-Phase APF. *Front. Energy Res.* **2021**, *9*, 727364. [CrossRef]
23. Wu, L.; Liu, J.; Vazquez, S.; Mazumder, S.K. Sliding Mode Control in Power Converters and Drives: A Review. *CAA J. Autom. Sin.* **2022**, *9*, 392–406. [CrossRef]
24. Tan, S.-C.; Lai, Y.M.; Tse, C.K. Indirect Sliding Mode Control of Power Converters Via Double Integral Sliding Surface. *IEEE Trans. Power Electron.* **2008**, *23*, 600–611.
25. Komurcugil, H.; Biricik, S.; Bayhan, S.; Zhang, Z. Sliding Mode Control: Overview of Its Applications in Power Converters. *IEEE Ind. Electron. Mag.* **2021**, *15*, 40–49. [CrossRef]
26. Kde Carvalho, B.; Bezerra, T.M.; Rocha, N.; de Almeida, R.G.; Fernandes, D.A. Model Predictive Current Controller for Grid Connected Photovoltaic System Based on Four-Leg Inverter. In Proceedings of the 2023 IEEE 8th Southern Power Electronics Conference and 17th Brazilian Power Electronics Conference (SPEC/COBEP), Florianopolis, Brazil, 26–29 November 2023; pp. 1–7.
27. Zhao, Z.; Sha, Y.; Gong, M.; Zhu, Y.; Yang, Y.; Rodriguez, J. Research on Continuous Control Set Model Predictive Control of Three-Phase Four-Leg Inverter. In Proceedings of the 2024 IEEE 10th International Power Electronics and Motion Control Conference (IPEMC2024-ECCE Asia), Chengdu, China, 17–20 May 2024; pp. 1041–1045.
28. Tran, H.N.; Dzung, P.Q.; Le, N.A.; Nguyen, T.D. Dynamic voltage restorer-multilevel inverter based on predictive voltage controller. In Proceedings of the 2016 IEEE International Conference on Sustainable Energy Technologies (ICSET), Hanoi, Vietnam, 14–16 November 2016; pp. 174–179.